

AD-DAE: Unsupervised Modeling of Longitudinal Alzheimer's Disease Progression with Diffusion Auto-Encoder

Ayantika Das^a, Arunima Sarkar^a, Keerthi Ram^b, Mohanasankar Sivaprakasam^{a,b}, and for the Alzheimer's Disease Neuroimaging Initiative*

^a*Department of Electrical Engineering, Indian Institute of Technology Madras (IITM), Chennai 600036, Tamil Nadu, India,*

^b*Sudha Gopalakrishnan Brain Centre, IITM, Chennai 600036, Tamil Nadu, India,*

Abstract

Generative modeling frameworks have emerged as an effective approach to capture high-dimensional image distributions from large datasets without requiring domain-specific knowledge, a capability essential for longitudinal disease progression modeling. Recent generative modeling approaches have attempted to capture progression by mapping images into a latent representational space and then controlling and guiding the representations to generate follow-up images from a baseline image. However, existing approaches impose constraints on distribution learning, leading to latent spaces with limited controllability to generate follow-up images without explicit supervision from subject-specific longitudinal images.

In order to enable *controlled* movements in the latent representational space and generate progression images from a baseline image in an *unsupervised* manner, we introduce a conditionable *Diffusion Auto-encoder* framework. The explicit encoding mechanism of image-diffusion auto-encoders forms a compact latent space capturing high-level semantics, providing means to disentangle information relevant for progression. Our approach leverages this latent space to condition and apply **controlled shifts** to baseline repre-

*Data used in preparation of this article were obtained from the Alzheimer's Disease Neuroimaging Initiative(ADNI) database adni.loni.usc.edu). As such, the investigators within the ADNI contributed to the design and implementation of ADNI or provided data but did not participate in the analysis or writing of this report. A complete listing of ADNI investigators can be found at: <https://adni.loni.usc.edu/wp-content/uploads/>

**Corresponding Author

Email address: dasayantika486@gmail.com (Ayantika Das)

sentations for generating follow-up. Controllability is induced by restricting these shifts to a subspace, thereby **isolating** progression-related factors from subject identity-preserving components. The shifts are implicitly guided by correlating with progression attributes (age and cognitive status), **without** requiring subject-specific longitudinal **supervision**. We validate the generations through image quality metrics, volumetric progression analysis, and downstream classification in Alzheimer’s disease datasets from two different sources and disease categories. This demonstrates the effectiveness of our approach for Alzheimer’s progression modeling and longitudinal image generation.

Keywords: Alzheimer’s Disease, Denoising Diffusion Model, Unsupervised, Latent Representation, Disentanglement

1. Introduction

Anatomical changes in the brain across a longitudinal time span, exceeding the rate of change in normal aging, are a crucial indicator for neurodegenerative disease, like Alzheimer’s. Structural MRI provides radiological features to observe and assess the nature of the disease progression (McKhann et al., 2011),(Jack Jr et al., 2024). In clinical practice, longitudinal assessment is performed by acquiring an MRI image of a current time point (follow-up) and comparing it against a previous time point (baseline) (Barnes et al., 2009). These comparisons are performed by segmenting specific brain regions known to be involved in Alzheimer’s, followed by quantifying volumetric differences, and quantification of regional changes applying voxel-based morphometry (Ashburner and Friston, 2000).

In contrast to progression assessment, **progression modeling** involves learning time- and disease-state dependent changes as observed in a training dataset of longitudinal MRI images of multiple subjects (individuals). The model is expected to capture the joint distribution of the image, the age at imaging, and disease state of all subjects within the dataset. Further, **generative models for progression** use such distribution learning and offer the capability to sample from an inferred conditional distribution of the possible follow-up image given a baseline image, conditioned on the anticipated disease state and age. This offers a unique possibility of predicting future time point images.

Generative modeling approaches like Variational auto-encoder (**VAE**), have been applied to capture image distributions and generate follow-up

images across longitudinal time spans. VAEs map images to a latent representational vector space that is regularized towards a desired prior distribution. The decoder of the VAE maps the latent vector embedding back to the image domain using an auto-encoding data term. While this approach drives the latent space towards encoding image details, VAEs may result in blurry and low-fidelity image generations that may not completely preserve the subject identity vis-a-vis the input image. Therefore prior works use an external modeling module that learns disease trajectories either from group-level trends or from subject-specific longitudinal data (Sauty and Durrleman, 2022), (Marti-Juan et al., 2023).

Generative Adversarial Networks (**GAN**) have also been widely utilized to capture MRI brain image distribution and generate plausible future follow-up images. The temporal trajectory for follow-up image generation is captured by guiding and conditioning the baseline image representations either with direct supervision from subject-specific longitudinal data or with self-supervision. Self-supervised techniques include baseline to follow-up generation by introducing controlled changes correlated with progression attributes like age difference, while constraining the transformation to remain close to the baseline (Xia et al., 2021), (Wang et al., 2023), (Pombo et al., 2023).

Unlike GANs which learn distribution mapping of input to output, auto-encoder models like VAE work with a latent representational space, where all subject images are mapped to points in the latent space. We seek to utilize this capability, which makes disease and age-related changes explainable as *movements* or a simple translation of points in the latent space. Further, we require a structured organization of the latent space, to achieve a subspace for normal aging related changes and a disentangled subspace for conditional manipulation of the representation. Our desired approach is a generative model that involves **capture** of image distribution from multiple *time points* and disease states into a **controllable representational space**, such that *movement* in the representational space can generate temporal progression.

The **Denoising Diffusion**-based recent generative approaches have been employed to capture and generate Alzheimer’s disease progression. The **latent diffusion** models operate on the latent space of an encoder-decoder model, to learn representations of follow-up images by integrating progression-related attributes (Puglisi et al., 2024). This formulation provides a flexible integration of progression attributes in the latent space, allowing better control over the temporal trajectory movement. However, this controllability and its effect on the generated follow-up images are dependent on the encoder-decoder model’s ability to capture the image distribution.

In order to better capture the image distribution while having a con-

trollable latent representational space, we propose to introduce a **Diffusion Auto-encoder** (DAE) model consisting of an image encoder and a diffusion decoder for the task of modeling brain MRI images. The denoising component of the decoder learns to generate images from pure Gaussian noise, guided by the latent representations produced by the encoder (Preechakul et al., 2022). This design ensures that the encoded representations remain explicit and compact, thereby facilitating the disentanglement of information within the latent space (Hudson et al., 2024). Such a formulation has motivated the application of DAE models to multiple image transformation tasks with only limited supervision. However, current approaches do not provide effective means to perform **localized** and **controlled** movements in the latent space—capabilities essential for modeling longitudinal progression of diseases in an **unsupervised** manner.

We propose to generate longitudinal progression in MRI brain images by enabling **controlled** movements within the latent representational space of the DAE framework, ensuring **disentanglement** of subject identity-preserving components and learning **without** explicit **supervision** from the subject-specific images. Our contributions can be summarized as:

1. We introduce **AD-DAE**, a Diffusion Auto-encoder-based framework to generate Alzheimer’s disease progression, by inducing **controlled shifts** in latent representation space, precisely guiding the generation of progression follow-up from baseline images. The controlled shifts ensure **disentanglement** of progression-specific factors from the subject identity-preserving components.
2. We further devise an **unsupervised** mechanism to learn the direction and magnitude of movement of the latent shifts by correlating with progression attributes rather than dependence on subject-specific images.
3. We validate our approach on 1016 subjects from ADNI and OASIS datasets by (i) quantifying generation quality along with generalization capability, using image metrics and qualitative progression visualizations; (ii) evaluating volumetric measures of disease-specific regions and assessing deformation captured within the generated images; and (iii) analyzing latent disentanglement.

2. Related Works

Our approach can be categorized as a condition-driven diffusion modeling, designed to generate longitudinal brain MRI images without paired

subject-specific supervision. Relating to our contribution, we discuss the following: (i) Generative approaches for progression modeling, focusing on how progression is encoded, (ii) Diffusion-based methods for progression generation, and (iii) unsupervised image-to-image translation.

2.1. Generative Approaches for Longitudinal Data Generation

Conditional generative frameworks that directly integrate progression attributes and learn from subject-specific longitudinal data have largely been adopted for this task. GAN-based frameworks like mi-GAN (Zhao et al., 2020), 4D-DANI-Net (Ravi et al., 2022), and Identity-cGAN (Jung et al., 2021) employ biologically-informed and identity-preserving constraints along with subject-specific images to model the progression trajectory. Similar to GANs, VAE-based approaches like DE-CVAE (He et al., 2024) utilize a dual-encoder based approach to better model the progression attributes while being supervised with subject-specific images.

Among unpaired approaches, the Conditional Adversarial Auto-encoder (CAAE) (Zhang et al., 2017) initially demonstrated that traversals in the GAN latent space can generate age-progressed images without subject-specific supervision. Building upon this, IPGAN (Xia et al., 2021) and Identity-3D-cGAN (Jung et al., 2023) incorporated identity-preserving constraints to brain MRI, where adaptive losses enforce similarity to the baseline while progression is correlated with age or other attributes. Other approaches, such as CounterSynth (Pombo et al., 2023) and SITGAN (Wang et al., 2023), apply diffeomorphic transformations to baseline images guided by disease labels or progression attributes. While these approaches can generate progression data without subject-specific longitudinal supervision, in order to precisely capture the temporal trajectory, better distribution modeling approaches like diffusion models can be employed.

2.2. Diffusion Models for Longitudinal Data Modeling

Denoising diffusion models have been applied to longitudinal progression modeling at both the latent and image levels. *Latent diffusion* models such as BrLP (Puglisi et al., 2024) generate follow-up latent representations through transformation of baseline latents conditioned on multiple progression factors and supervised by subject-specific follow-ups. Further models like MRExtrap (Kapoor et al., 2024) guide the latent transformation by assuming linear, age-dependent trajectories from baseline to follow-up. Recently, inference-time longitudinal image generation approaches have been developed employing these latent diffusion models through guidance from time-progressed images of other subjects (Zhang et al., 2024).

While latent diffusion offers a compact representational space for conditioning, performance is constrained by the distribution capturing capability of the pre-trained encoder-decoder. In contrast, image-level diffusion directly models Gaussian noise in image space, allowing more precise control of the generated images. Among *image-diffusion* models, SADM (Yoon et al., 2023) incorporates a transformer to encode temporal dependencies across longitudinal images as a conditioning to the diffusion, and TADM (Litrico et al., 2024) predicts the additive residual to transform a baseline into a follow-up through diffusion denoising while regressing the age gap. While these approaches better capture the image distribution, they are mostly guided by subject-specific longitudinal images.

2.3. Diffusion Models for Unsupervised Image-to-Image Tasks

Latent representations of image diffusion models have been employed to achieve multiple unsupervised attribute manipulation tasks. Diffusion Deformable Model (Kim and Ye, 2022) and DiffuseMorph (Kim et al., 2022) estimate transformations by conditioning on reference subjects while preserving subject identity. The latent representations obtained from these modeling approaches enable progression generation in an unsupervised manner (Dalva and Yanardag, 2024). However, these latents are based on the conventional diffusion structures (Dhariwal and Nichol, 2021), residing in the time-dependent image space, and not enabling precise control. To address this, Diffusion Auto-encoders (DAE) (Preechakul et al., 2022), (Zhang et al., 2022) introduce a compact and structured latent space (Das et al., 2025), obtained through separate image encoding, which then directly guides the conventional UNet-based denoising process (Ho et al., 2020), (Nichol and Dhariwal, 2021).

The latent representations of DAEs have been employed in various attribute manipulation tasks (Huang et al., 2025). Without explicit guidance from the target, SSR-Encoder (Zhang et al., 2024) and PADA (Li et al., 2023) learns to integrate textual information with latent representations of DAE, to better guide the generation process. Further, HDAE (Lu et al., 2024) learns to generate mixed stylized images by combining latent representations of different subjects. Additionally, the DAE latents have been shown to disentangle attributes across different subsets of latent dimensions (Yue et al., 2024), (Hudson et al., 2024). While these methods show that DAE latent representations can compactly encode and isolate attributes, we propose to leverage this *latent space* for **unsupervised** disease progression generation through *controlled shifts* within the space, ensuring **disentanglement** of disease-related factors from subject identity.

3. Methodology

Our proposed approach AD-DAE is a Diffusion Auto-encoder (DAE)-based framework which generates disease progression images by introducing: (i) *Latent Shift Estimation* module, which induces controlled movements in the latent representational space of DAE to generate progression follow-up images from baseline; and (ii) *Consistency* module, which implicitly guides the latent movements by ensuring that changes between the baseline and generated follow-up images align with the required progression attributes. The architectural flow of our devised method is illustrated in Figure 1 and the algorithmic overview is given in Algorithm 1.

In the **DAE** formulation, the encoding (\mathcal{E}) component maps input images ($x \in \mathbb{R}^{h \times w}$) into latent representations ($z \in \mathbb{R}^d$), which guides the denoising diffusion component (\mathcal{D}) during image generation ($\hat{x} \in \mathbb{R}^{h \times w}$). This latent space enables us to devise a mechanism to generate disease progression images by shifting the progression-related dimensions of the DAE latent representation (z).

The **Latent Shift** required to generate a progression follow-up image (x_f) from a subject’s current baseline image (x_b) is estimated through a learnable module (\mathcal{A}) that maps progression attributes (cognitive status and age) into a latent shift vector (z'). This mapping ensures that the latent shift z' lies in the subspace of the latent representational space ($z_b = \mathcal{E}(x_b)$). The latent shift operation is confined within a subset (m) of the latent dimensions, allowing decoupling of progression-related factors from other subject-identity related factors of latent z_b . The resulting shifted latent representation further guides the denoising diffusion (\mathcal{D}) to generate a follow-up image (\hat{x}_f).

The **optimization** of the latent shift estimator (\mathcal{A}), without direct supervision from the true subject-specific follow-up image x_f , is achieved by introducing a consistency module (\mathcal{R}). The **Consistency** module (\mathcal{R}) regresses the progression attributes, ensuring consistency with the inputs of \mathcal{A} , given the baseline (x_b) and the generated follow-up (\hat{x}_f) as input. As \mathcal{R} learns to regress the progression attributes, the latent shift estimator \mathcal{A} is implicitly guided to produce semantically meaningful movements in the latent space, thereby enabling transformation of x_b into a progression image (\hat{x}_f).

The following subsections detail the modeling components of our proposed framework for Alzheimer’s progression (**AD-DAE**), (i) Diffusion Auto-encoder (Subsection 3.1), (ii) Latent Shift Estimation Module (Subsection 3.2), (iii) Regression Module (Subsection 3.3), along with the (iv) Training and Inference process (Subsection 3.4).

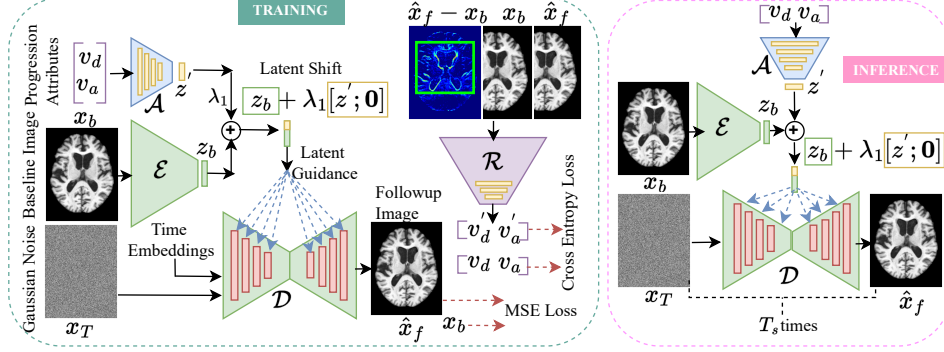


Figure 1: From left to right, the training and inference strategy is described. **Training Module:** From left to right, the baseline image (x_b), Gaussian noise (x_T), time embeddings (t) and the progression attributes (v_a, v_d) are processed through the encoder (\mathcal{E}), latent shift module (\mathcal{A}) and the decoder (\mathcal{D}). The latent vector (z_b) from \mathcal{E} gets shifted by z' incorporating progression factors and generating follow-up image (\hat{x}_f). The regression component \mathcal{R} processes x_b , \hat{x}_f , and their residual to estimate the progression attributes, while optimizing \mathcal{A} . **Inference Module:** Image x_b , noise, and progression attributes are processed T_s times to generate \hat{x}_f with latent shift integration.

3.1. Diffusion Auto-encoder (DAE)

At the core of our progression modeling approach is a diffusion-based auto-encoder, which has an encoding component (\mathcal{E}) and a denoising diffusion decoding component (\mathcal{D}).

3.1.1. Denoising Decoder (\mathcal{D})

The denoising decoder \mathcal{D} is an image-based diffusion that iteratively learns to transform a noise sample (x_T), drawn from a standard Gaussian distribution, into a target image (x_0) utilizing the DDIM (Song et al., 2020) strategy. This iterative transformation is the reverse of the forward diffusion process given by a time-dependent Gaussian distribution as,

$$q(x_t|x_{t-1}) = \mathcal{N}(\sqrt{1 - \beta_t}x_{t-1}, \beta_t I) \quad (1)$$

where β_t represents the noise levels. The diffusion process spans across total T time steps. At each time step t , the goal of $\mathcal{D}(x_t, t)$ is to model the reverse process ($p_\phi(x_{t-1}|x_t)$) given the noisy input x_t . This noisy image can be approximated using the following distribution,

$$q(x_t|x_0) = \mathcal{N}(\sqrt{\alpha_t}x_0, (1 - \alpha_t)I) \quad (2)$$

where $\alpha_t = \prod_{s=1}^t (1 - \beta_s)$ and $x_t = \sqrt{\alpha_t}x_0 + \sqrt{1 - \alpha_t}\epsilon$, $\epsilon \sim \mathcal{N}(0, I)$. The model \mathcal{D} is configured to directly estimate x_0 such that, $\hat{x}_0 = \mathcal{D}(x_t, t)$. With this configuration, the reverse process to be modeled is given by the distribution as,

$$p_\phi(x_{t-1} | x_t) = \begin{cases} \mathcal{N}(\mathcal{D}(x_1, 1), 0) & \text{if } t = 1 \\ q(x_{t-1} | x_t, \hat{x}_0) & \text{otherwise} \end{cases} \quad (3)$$

where $q(x_{t-1} | x_t, \hat{x}_0)$ is derived from equation 1 and 2, and is given as,

$$q(x_{t-1} | x_t, \hat{x}_0) = \mathcal{N}(\sqrt{\alpha_{t-1}}\hat{x}_0 + \sqrt{1 - \alpha_{t-1}}(\frac{x_t - \sqrt{\alpha_t}\hat{x}_0}{\sqrt{1 - \alpha_t}}), 0) \quad (4)$$

This formulation allows the reverse denoising process to sample x_{t-1} given x_t in a tractable manner. The entire pipeline is implemented through a convolution UNet (Ho et al., 2020), (Song et al., 2020). This UNet, in the denoising process, serves as a decoder in the DAE module, being conditioned on latent representations from the integrated encoder (\mathcal{E}), which is detailed below.

3.1.2. Guiding Encoder (\mathcal{E})

The denoising decoder (\mathcal{D}) is guided by the latent representation produced by the encoder ($z = \mathcal{E}(x_0)$), enabling an auto-encoding-like (Preechakul et al., 2022) structure ($\hat{x}_0 = \mathcal{D}(x_t, t, z)$) during the iterative image generation process. The guidance from the encoder (\mathcal{E}) is integrated into \mathcal{D} by conditioning each of its layers through activation modulation. These activations within \mathcal{D} are first normalized via group normalization and then modulated using learned scale and bias parameters derived from z .

The latent space offered by the encoder \mathcal{E} enables image transformation in an unsupervised manner since the latent representations (z) can encapsulate meaningful information. This is primarily because the denoising process specializes in reconstructing **high-frequency** details, allowing the encoded latent representation to focus on capturing high-level **semantic** structures (Hudson et al., 2024). In contrast, conventional auto-encoders require the latent space to encode both low-level details and high-level semantics within a single representation.

By decoupling these factors, our framework enables the latent representations to emphasize on structural regions, such as the ventricles and hippocampus, which are affected by Alzheimer’s progression. In order to introduce changes in these regions and generate progression images, shift is incorporated in the latent representation of DAE through the latent shift estimation module \mathcal{A} as detailed below.

Algorithm 1 AD-DAE Training

```

1: Input: Baseline image  $x_b \in \mathbb{R}^{h \times w}$ , progression attributes  $(v_d, v_a)$ , parameters
    $\lambda_1, \lambda_2, \lambda_3$ , time steps  $T$ 
2: Output: Follow-up image  $\hat{x}_f \in \mathbb{R}^{h \times w}$ 
   Training:
3: Initialize  $\mathcal{E}, \mathcal{D}, \mathcal{A}, \mathcal{R}$ 
4: Auto-encoding Mode ( $\lambda_1 = 0$ ):
5: for epochs 1 to 50 do
6:   Encode  $z_b = \mathcal{E}(x_b)$ 
7:   Generate  $\hat{x}_b = \mathcal{D}(x_t, t, z_b)$ ,  $t = 1, \dots, T$ 
8:   Optimize  $\mathcal{L}_{MSE} = \|x_b - \hat{x}_b\|_2^2$ 
9: end for
10: Progression Mode ( $\lambda_1 = 1$ ):
11: for epochs 1 to 100 do
12:   Encode  $z_b = \mathcal{E}(x_b)$ 
13:   Estimate shift  $z' = \mathcal{A}(v_d, v_a)$ , where  $v_d^{k_i}, k_i \in \{1, 2, 3\}$ ,  $v_a^{k_j}, k_j \in \{4, \dots, 13\}$ 
14:   Compute  $z'_f = z_b + [z'; \mathbf{0}]$ ,  $z' \in \mathbb{R}^m$ ,  $\mathbf{0} \in \mathbb{R}^{d-m}$ 
15:   Generate  $\hat{x}_f = \mathcal{D}(x_t, t, z'_f)$ ,  $t = 1, \dots, T$ 
16:   Compute residual  $r = x_b - \hat{x}_f$ 
17:   Regress attributes  $(v'_d, v'_a) = \mathcal{R}(x_b, \hat{x}_f, r)$ 
18:   Optimize  $\mathcal{L} = \lambda_2 \mathcal{L}_{MSE} + \lambda_3 \mathcal{L}_{CE}$ , where  $\mathcal{L}_{CE} = -\mathbf{v}_d^\top \log \mathbf{v}'_d - \mathbf{v}_a^\top \log \mathbf{v}'_a$ 
19: end for

```

3.2. Latent Shift Estimation Module

The latent shift estimation module \mathcal{A} of our model AD-DAE estimates the shift required to generate a progression follow-up image (\hat{x}_f) of a baseline image x_b . The latent shift (z') is introduced through an additive operation on the latent representation z_b ($z_b = \mathcal{E}(x_b)$) to estimate the follow-up latent representation (z'_f). This estimated representation is employed to predict the follow-up image given by $\hat{x}_f = \mathcal{D}(x_t, t, z'_f)$.

Input Attributes: The shift estimation module \mathcal{A} takes the progression attributes, (i) age gap (v_a) between the baseline and follow-up, and (ii) the cognitive status (v_d) as input. The progression attributes are represented by one-hot vectors as, $(v_d^{k_i}, v_a^{k_j}) = ((0, \dots, 1_{k_i}, \dots, 0), (0, \dots, 1_{k_j}, \dots, 0))$, where k in $v_d^{k_i}$ and $v_a^{k_j}$ indicates the positions indicating each of the cognitive sub-types and age-gaps respectively. The three cognitive statuses are CN, MCI, and AD, and the age gaps are of 0.5 years each, giving the capability to progress through 5 years of age gap.

The latent shift module processes these progression attributes and produces the required latent shift $z' = \mathcal{A}(v_d, v_a)$, which captures cognitive and age-related movements in the latent space of DAE. The shift vector ($z' \in \mathbb{R}^m, m < d$) is added to a subset of the latent z_b through the following

operation, $z'_f = z_b + [z'; \mathbf{0}]$, where $z' \in \mathbb{R}^m$ and $\mathbf{0} \in \mathbb{R}^{d-m}$. This shift in the first m elements of the d latent dimensions of z_b ensures progression-relevant attributes are **decoupled** from the subject-specific identity features encoded in the remaining $d - m$ dimensions. This isolation of progression-specific properties enables the generated follow-up image (\hat{x}_f) to reflect structural changes, such as enlargement or shrinkage, associated with progression, while preserving identity-relevant anatomical structures.

3.3. Consistency Module

In order to **optimize** the latent shift estimation module (\mathcal{A}) and generate meaningful shifts in the latent space, a consistency module (\mathcal{R}) is introduced which extracts features from the (i) baseline image (x_b) (ii) predicted follow-up image (\hat{x}_f) and (iii) their residual ($x_b - \hat{x}_f$), to regress the progression attributes, $(v'_d, v'_a) = \mathcal{R}(x_b, \hat{x}_f, x_b - \hat{x}_f)$. The module \mathcal{R} focuses on the changes introduced between x_b and \hat{x}_f and estimates progression attributes (v'_d, v'_a) , while enforcing the estimations to be consistent with the input progression attributes (v_d, v_a) . This ensures that the latent shift vector z' ($\hat{x}_f = \mathcal{D}(x_t, t, z_b + [z'; \mathbf{0}])$) generates \hat{x}_f by **correlating** with the estimated progression attributes (v'_d, v'_a) .

While \mathcal{R} encourages transformation of x_b to \hat{x}_f , the generated changes remain controlled since, (i) z' is added to only first m dimensions of z_b , while the remaining $(d - m)$ dimensions are preserved to retain identity-specific properties of x_b in \hat{x}_f ; (ii) the residual $x_b - \hat{x}_f$ is masked to emphasize only on the changes restricted to progression-related regions (ventricles, hippocampus, and amygdala); and (iii) similarity between x_b and \hat{x}_f is enforced with MSE loss discussed in the Subsection 3.4. The residual mask is obtained by segmenting regions (r) of interest from x_b and \hat{x}_f , followed by constructing a bounding box covering all segmented regions across both images.

3.4. Training And Inference

3.4.1. Training Objectives Functions

The DAE module of our model is primarily optimized with MSE loss function $\mathcal{L}_{MSE} = \|x_b - \hat{x}_0\|_2^2$, where $\hat{x}_0 = \mathcal{D}(x_t, t, z_b + \lambda_1[z'; \mathbf{0}])$. The regression module (\mathcal{R}) is optimized by a cross-entropy-based objective function given as, $\mathcal{L}_{CE} = -\mathbf{v}_d^\top \log \mathbf{v}'_d - \mathbf{v}_a^\top \log \mathbf{v}'_a$. The overall objective function is given as,

$$\mathcal{L} = \begin{cases} \mathcal{L}_{MSE}, & \text{if } \lambda_1 = 0 \\ \lambda_2 \mathcal{L}_{MSE} + \lambda_3 \mathcal{L}_{CE}, & \text{if } \lambda_1 = 1 \end{cases} \quad (5)$$

The parameter λ_1 enables the model to alternate between two modes: auto-encoding ($\hat{x}_0 = \hat{x}_b$) when $\lambda_1 = 0$, and progression generation ($\hat{x}_0 = \hat{x}_f$) when $\lambda_1 = 1$. The model is trained in auto-encoding mode for initial few epochs for learning to extract meaningful features for any given MRI image.

In progression generation mode, the loss term \mathcal{L}_{CE} ensures that the changes induced in \hat{x}_f by the latent shift z' allow \mathcal{R} to regress attributes (v'_d, v'_a) , and enforce consistency with the input attributes (v_d, v_a) , ensuring that the latent shift estimated by \mathcal{A} is optimized toward generating meaningful follow-up images. This drives convergence of the consistency module and enforces a non-sparse latent shift z' . While it supports unsupervised generation of progressive images, \mathcal{L}_{MSE} supports meaningful reconstruction and identity preservation. The parameters λ_2 and λ_3 balance allowable transformations against these constraints.

3.4.2. Inference

During inference, a subject’s baseline image x_b is first encoded by the encoder \mathcal{E} to obtain the latent representation z_b . This latent is then shifted by z' , which is estimated based on the progression attributes $(\mathbf{v}_d, \mathbf{v}_a)$, resulting in a modified latent vector (z'_f) that guides the decoder \mathcal{D} to generate the follow-up image \hat{x}_f . The denoising decoder ($\mathcal{D}(x_t, t, z'_f)$) iteratively samples the follow-up image \hat{x}_f , initiating from x_T and guided by $z'_f = z_b + [z'; \mathbf{0}]$, following equations 3 and 4. The iterative sampling is performed for T_s time steps.

4. Experimental Setup

4.1. Datasets

We have utilized longitudinal brain MRI images from the Alzheimer’s Disease Neuroimaging Initiative (ADNI) (adni.loni.usc.edu) (Jack Jr et al., 2008) and Open Access Series of Imaging Studies (OASIS) (oasis-brains.org) (LaMontagne et al., 2019) repositories. The images considered from both repositories were T1-weighted 3D images. **ADNI:** From ADNI repository, we have considered subjects from three different cognitive statuses: cognitively normal (CN), mildly cognitively impaired (MCI), and AD. The images utilized were within the age range of 63 – 87 years and across all gender specifications. The images considered had undergone gradient inhomogeneity and bias corrections and were labeled as *MPR*; *GradWarp*; *B1 Correction*; *N3*. The average age difference between baseline and follow-up images was 2.93 ± 1.35 years. **OASIS:** Similar to the ADNI from OASIS repository, we have

Table 1: Parameter Details

Parameters	Values	Parameters (contd.)	Values (contd.)
Epochs	Auto-encode: 50 Progression: 100	Latent Dimensions (d, m)	512, 50
Axial Height (H), Width (W), Slices (D)	208, 160, 100	λ_1	Auto-encode: 0 Progression: 1
Optimizer	Adam	λ_2, λ_3	1, 0.001
Learning Rate	0.001	Cognitive Types: $v_d^{k_i}$ $(0, \dots, 1_{k_i}, \dots, 0)$	$k_i \in \{1, 2, 3\}$
Diffusion Noise (β_t, T, T_s)	Linear Scheduling, 1000, 50	Age Gap: $v_a^{k_j}$ $(0, \dots, 1_{k_j}, \dots, 0)$	$k_j \in \{4, \dots, 13\}$
\mathcal{E}, \mathcal{D}	ResNet, UNet(Preechakul et al., 2022)	Region Segmentation (r)	SynthSeg(Billot et al., 2023)
\mathcal{R}	ResNet, MLP layers	Jacobian-based Analysis	ANTs ¹
\mathcal{A}	MLP Layers, Activations	Disease Classification	ResNeXt(Xie et al., 2017), MLP Layers

¹ ANTs Jacobian

utilized data from the cognitively normal, MCI due to AD, and AD dementia groups. The age range of the images was within 60 – 90 years with various gender specifications. The average age difference was 3.13 ± 1.52 years.

4.2. Evaluation Metrics

Image Quality Metrics: To evaluate the similarity between generated follow-up images (\hat{x}_f) and ground-truth follow-up images (x_f), standard image-based measures are employed. We calculate Peak Signal-to-Noise Ratio (PSNR), Structural Similarity Index (SSIM), and Mean Squared Error (MSE) between \hat{x}_f and x_f . **Volumetric Analysis:** To assess how well progression is modeled in 3D volumes, we compare errors between the volumetric estimates of generated and ground truth images. We measure region-wise Mean Absolute Error (MAE) between $(V_{\hat{X}_f}^r - V_{X_b}^r)/(V_{X_b}^r)$ and $(V_{X_f}^r - V_{X_b}^r)/(V_{X_b}^r)$, where V_X^r is the sum of voxels belonging to region r ($r \in$ Hippocampus/ Amygdala/ Lateral Ventricular) in any 3D image volume (X). The region-wise estimates are extracted by segmenting the 3D image volumes. We further measure the difference between the deformations required to transform the generated follow-up ($\hat{X}_f \rightarrow X_b$) and the ground-truth follow-up ($X_f \rightarrow X_b$) to the baseline image. The difference is quantified with region-wise MAE between the Jacobian determinants of

both the deformation fields, represented as, $\text{MAE}(J_{\hat{X}_f \rightarrow X_b}, J_{X_f \rightarrow X_b})$. The transformation fields are estimated by diffeomorphic non-rigid registration using ANTs¹. **Disease Classification Analysis:** To determine how the generated data augments the true training distribution and impacts classification, we trained disease classifiers with varying ratios of real and generated samples.

4.3. Implementation Details

4.3.1. Dataset Details

From the ADNI dataset, we constructed a *Train Set* of 486 subjects (179 CN, 160 MCI, 147 AD) and a *Test Set* of 466 subjects (159 CN, 156 MCI, 151 AD). A *Latent Swap Set* was created by pairing CN and AD subjects of similar age (within 0.5 years). In a pair, the age gap associated with the AD subject is of two years or more, and with the CN subject is less than two years. In addition, a *Cross-Data Setup* was created with the unseen OASIS dataset, consisting of 550 subjects (330 CN, 137 MCI, 83 AD). All brain MRIs were pre-processed using skull stripping (Isensee et al., 2019), affine registration to MNI space, and intensity normalization (Shinohara et al., 2014).

4.3.2. Model Details

The models were implemented in PyTorch version 2.0.1 on an 80 GB NVIDIA A100 GPU and CUDA Version: 12.1. All the parameter details related to AD-DAE, and downstream analysis with region segmentation, and disease classification models are listed in Table 1. The code-base is made available at https://github.com/ayantikadas/AD_DAE.

Baseline Methods: The comparative baselines were chosen across various generative mechanisms. A supervised **VAE**-based approach, DE-CVAE (He et al., 2024), employing a dual-encoder design to model progression. Unsupervised conditional **GAN** methods, including CAAE (Zhang et al., 2017) and IPGAN (Xia et al., 2021), leverage unpaired longitudinal data from other subjects to generate follow-ups while preserving subject identity. A similar strategy is extended to a transformer-based cycle-GAN architecture in UVCGAN (Torbunov et al., 2023). SITGAN (Wang et al., 2023) represents another unsupervised GAN that learns progression by correlating image deformation with age and cognitive status. Further, we include a **latent diffusion** approach, BrLP (Puglisi et al., 2024), which integrates

¹<https://antspy.readthedocs.io/en/latest/registration.html>

multiple progression attributes to learn progression through guidance from subject-specific follow-ups. All baseline implementations were obtained from their official repositories: DE-CVAE ², (CAAE, IPGAN, & SITGAN) ³, UVCGAN ⁴, and BrLP ⁵. The model implementations were directly adopted from their source codes, and for fair comparison, the progression attributes used for all the models are cognitive-state, age, and region-level information from the hippocampus, amygdala, and lateral ventricles.

Table 2: Quantitative evaluation of AD-DAE against baseline methods on the *Test Set*, using image quality metrics (PSNR, SSIM, MSE) for progression prediction. Model size and inference time per 3D image (X) are also reported. Statistical significance ($p < 0.01$) is indicated by asterisk (*).

Methods	PSNR (dB) (\uparrow)	SSIM (\uparrow)	MSE (\downarrow)	Mod. Size/ Inf. Time
	CN/ MCI & AD	CN/ MCI & AD	CN/ MCI & AD	(MB/s)
Naive Baseline	27.25 \pm 2.12/ 26.75 \pm 2.07	0.93 \pm 0.021/ 0.92 \pm 0.021	0.0021 \pm 0.001/ 0.0024 \pm 0.001	-
CAAE (Zhang et al., 2017)	21.21 \pm 0.73/ 21.03 \pm 0.80	0.53 \pm 0.033/ 0.52 \pm 0.035	0.0077 \pm 0.001/ 0.0080 \pm 0.001	52.30/ 2.56
IPGAN (Xia et al., 2021)	25.86 \pm 2.12/ 25.31 \pm 2.13	0.92 \pm 0.032/ 0.91 \pm 0.034	0.0030 \pm 0.001/ 0.0034 \pm 0.002	52.30/ 2.34
UVCGAN (Torbunov et al., 2023)	26.43 \pm 2.57/ 25.13 \pm 1.53	0.92 \pm 0.033/ 0.91 \pm 0.031	0.0025 \pm 0.001/ 0.0041 \pm 0.001	122.90/ 5.24
BrLP (Puglisi et al., 2024)	26.71 \pm 1.02/ 26.20 \pm 1.14	0.79 \pm 0.022/ 0.79 \pm 0.025	0.0029 \pm 0.001/ 0.0030 \pm 0.001	576.76/ 13.38
DE-CVAE (He et al., 2024)	27.32 \pm 2.98/ 26.99 \pm 2.83	0.65 \pm 0.090/ 0.63 \pm 0.082	0.0023 \pm 0.001/ 0.0024 \pm 0.001	648.12/ 3.89
SITGAN (Wang et al., 2023)	28.73 \pm 3.25/ 28.09 \pm 3.23	0.94 \pm 0.033 / 0.93 \pm 0.034	0.0019 \pm 0.001/ 0.0022 \pm 0.001	98.78/ 5.08
AD-DAE	30.10* \pm 3.05 / 29.43* \pm 3.14	0.94* \pm 0.033 / 0.94* \pm 0.031	0.0017* \pm 0.001 / 0.0019* \pm 0.001	129.18/ 10.03

5. Results and Discussion

The results of quantitative evaluations on the ADNI *Test Set* and the OASIS *Cross-Data Setup* with image-level metrics are presented in Subsections 5.1 and 5.3. Qualitative analyses of age and cognitive status-related

²https://github.com/rosie068/Double_Encoder_CVAE_AD

³<https://github.com/clintonjwang/spatial-intensity-transforms>

⁴<https://github.com/LS4GAN/uvcgan>

⁵<https://github.com/LemuelPuglisi/BrLP>

progression for the ADNI *Test Set* are discussed in Subsection 5.2. Volumetric assessments at the 3D level are reported in Subsection 5.4. Downstream disease classification performance is discussed in Subsection 5.5. Further, latent space analyses of AD-DAE validating the disentanglement of progression factors from subject-identity are elaborated in Subsection 5.6.

5.1. Quantitative Analysis

The results of quantitative evaluation on the ADNI test set are presented in Table 2 using the image-level metrics PSNR, SSIM, and MSE. From the table, it is inferable that AD-DAE achieves an improvement of 1.37 dB and 1.34 dB in PSNR, along with MSE reductions of 0.0002 and 0.0003 across the cognitive categories, when compared to the better performing baseline SITGAN. In terms of SSIM, AD-DAE achieves a 0.01 gain over SITGAN for the MCI & AD category and shows comparable performance for the CN category. These improvements demonstrate that AD-DAE generates images with relevant anatomical changes, effectively capturing the true progression trajectories. The relatively lower performance of SITGAN as compared to AD-DAE can be attributed to its modeling formulation, which introduces progression implicitly without enforcing the internal representations to align with progression-specific changes.

Among other comparative models, the VAE-latent diffusion-based (BrLP) and dual-encoder VAE (DE-CVAE) approaches achieve lower image-level metric scores compared to AD-DAE, since their VAE formulations do not ensure transfer of progression-specific structural changes into the decoded image space. Despite supervision with subject-specific longitudinal scans, the performance of these approaches remains limited by distributional constraints. The GAN-based unsupervised approaches (CAAE, IPGAN, UVC-GAN) lack explicit progression disentanglement, resulting in lower overall performance. All baselines except SITGAN and DE-CVAE perform lower than the Naive Baseline, which directly compares true baseline and follow-up images, as variability in their generated images often exceeds progression-related changes. The image quality metrics decline from CN to MCI and AD across all models, reflecting the increased anatomical alterations with AD severity. In terms of model size and inference time, although diffusion models are heavier and slower, AD-DAE has reduced model size and faster inference than latent diffusion based BrLP. Overall, AD-DAE **performs better** than all the comparative baselines, demonstrating that it is more effective to model progression, ensuring that the internal latent representations **disentangle** the factors of generation.

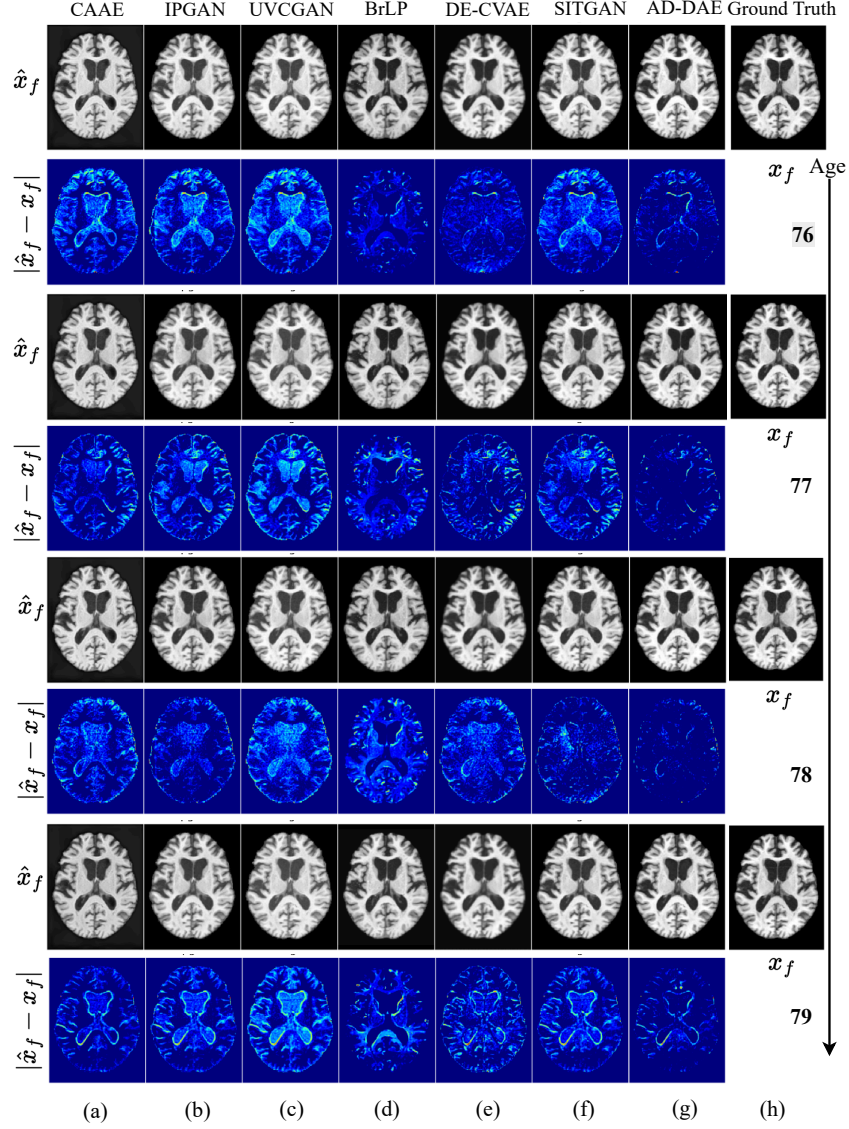


Figure 2: From left to right, columns (a)–(g) show predicted follow-up images (\hat{x}_f) with their error maps ($|\hat{x}_f - x_f|$) for AD-DAE and baseline methods, and column (h) shows the ground truth follow-up images (x_f). Results are shown for a subject from the MCI category (*Test Set*) with a baseline age of 75 years and a four-year age span (76–79 years). The error maps from AD-DAE exhibit relatively lower errors compared to other models.

5.2. Qualitative Analysis

The qualitative evaluations of AD-DAE compared to other methods are presented in Figure 2. The ground-truth follow-up (x_f) and generated images (\hat{x}_f) are shown for a four-year age gap (76–79 years), given a baseline of 75 years. From the figure, it is observed that AD-DAE demonstrates relatively lower absolute error between generated and ground-truth follow-up images compared to other approaches. This improvement stems from its ability to better preserve subject-specific details while generating progression-relevant anatomical changes. SITGAN shows relatively higher errors due to limited control over progression, with errors particularly larger at higher age gaps.

Among the other comparative models, DE-CVAE shows relatively lower errors for smaller age gaps but increases with larger progression intervals, as the generation of more anatomical changes often produces blurriness due to its VAE-based formulation. Similarly, BrLP shows higher errors at larger age gaps, as it also relies on a VAE-based decoder along with the latent diffusion. While progression is modeled explicitly, the lack of precise control in the image space results in reduced preservation of subject identity. The other GAN-based unsupervised models (CAAE, IPGAN, UVCGAN) capture progression less effectively, primarily due to the lack of explicit control by progression attributes in their formulations. Overall, AD-DAE generates ***progression-related features better*** than other comparative models, by explicitly enforcing subject-identity preservation in its latent representations and leveraging an image-based diffusion formulation. This enables generation of ***subject-specific*** properties while accurately modeling progression-related structural changes.

5.2.1. Anatomical Changes with Age Progression

To evaluate how effectively progression attributes were modeled, we considered a baseline image at age 75 from the MCI category and extracted the difference of predicted follow-up with ground-truth baseline images for ages 76 to 79 across different approaches, as shown in Figure 3. The first column (Figure 3(a)) represents the ground-truth progression, where difference maps derived from baseline and follow-up images highlight the ventricular enlargement increasing with age gap. Our approach closely follows this progression hierarchy (ventricular enlargement), showing smaller changes at lower age gaps and larger changes at higher gaps. SITGAN also models progression, capturing the enlargements in ventricular regions, but does not consistently maintain the hierarchy. The difference maps from SITGAN indicate changes beyond the ventricular regions, likely due to its formulation that introduces

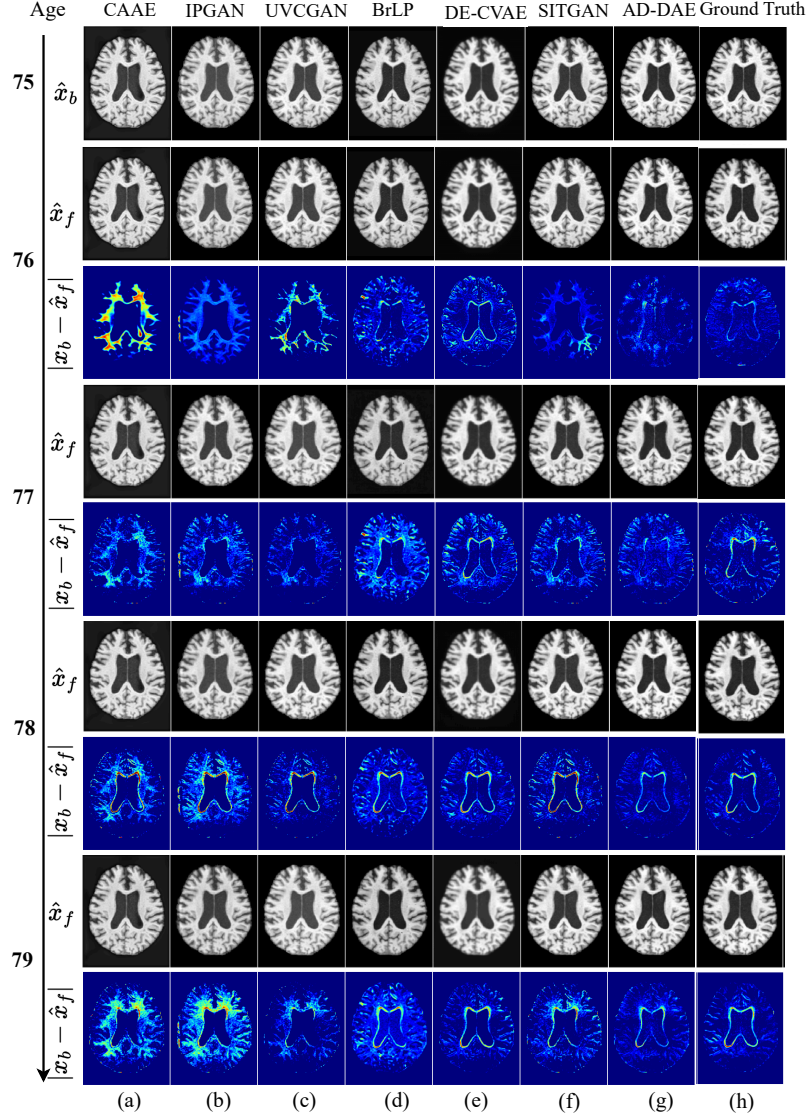


Figure 3: From left to right, columns (a)–(g) show the generated baseline (\hat{x}_b), follow-up (\hat{x}_f), and progression-related changes through the difference ($|\hat{x}_b - \hat{x}_f|$) for AD-DAE and comparative methods; column (h) shows the ground-truth baseline and follow-up. Results are from a subject of MCI category (*Test Set*), with a baseline age of 75 years and a four-year progression span (76–79 years). The difference maps indicate that AD-DAE captures the progression hierarchy relatively closer to the ground-truth progression changes.

additional intensity variations. DE-CVAE is able to capture the progression hierarchy, but often produces ventricular enlargements greater than the ground truth. This is primarily due to the lack of precise control of the progression-related factors. BrLP similarly reflects the progression hierarchy, but interference from other regions arises due to its VAE-diffusion formulation that introduces variability unrelated to progression. The other GAN-based unsupervised models (CAAE, IPGAN, UVCGAN) produce difference maps with scattered changes across the image, lacking meaningful localization and faithful generation of progression hierarchy. Overall, AD-DAE is able to *better* generate the *progression hierarchy*, introducing changes *focused* on *progression-relevant* regions.

5.2.2. Progression Analysis with Cognitive Status Variation

In order to evaluate how progression is modeled across different cognitive statuses, we have considered three subjects with similar baseline (82 years) and follow-up (84 years) ages from three progression categories, and evaluated the error between generated and true follow-up images, as shown in Figure 4. The figure shows that our AD-DAE approach achieves relatively lower errors compared to other methods, with errors increasing proportionally to progression severity due to larger anatomical changes. In our approach, the subject-specific properties that are not correlated with progression are preserved well compared to the baseline methods. Although SITGAN has a relatively higher error rate than our method, it has attempted to preserve the subject-related properties. BrLP and DE-CVAE yield comparable errors across all categories, but these errors are distributed across both progression-related and unrelated regions, with less localization to clinically relevant structures. In contrast, the other GAN-based approaches (CAAE, IPGAN, UVCGAN) show errors that do not align with the progression hierarchy and are concentrated in progression-specific regions. Within the AD category, supervised models capture progression better than unsupervised approaches. Overall, AD-DAE shows relatively *lower errors* than other methods, preserving *subject-related* details and introducing changes *correlated* with *disease severity*.

5.3. Performance in Cross-Data Setup

To evaluate generalization capability, we tested the model in a *Cross-Data Setup* using OASIS data. Performance was assessed with PSNR, SSIM, and MSE, and the results are summarized in Figure 5, which reports cognitive state-wise comparisons between AD-DAE and the baseline methods. Across all metrics, AD-DAE achieves relatively better or comparable performance

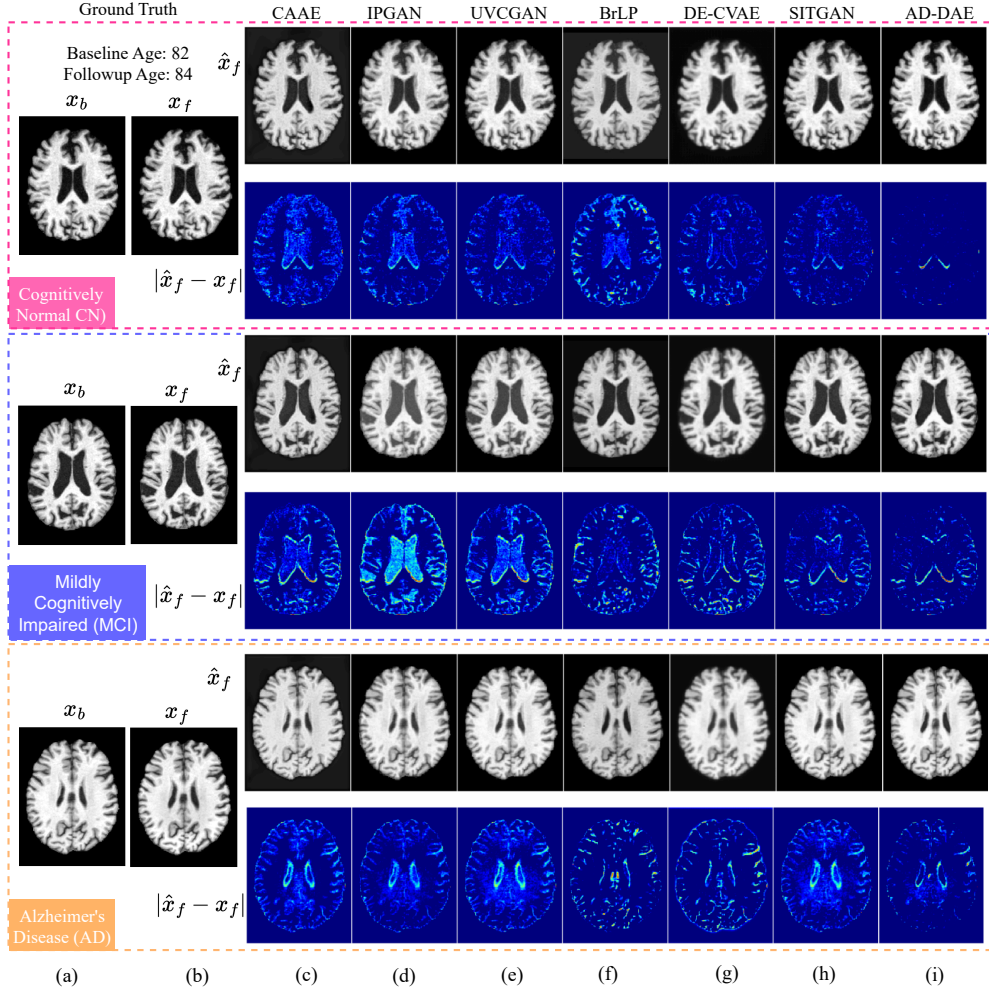


Figure 4: Top to bottom: From *Test Set* images and error maps for CN, MCI, and AD cohorts. Left to right: (a) Ground truth baselines (age 82), (b) Ground truth follow-ups (age 84), (c)–(i) Generated follow-up images and error maps (relative to ground truth follow-up) for AD-DAE and baseline methods. Overall, AD-DAE shows relatively lower errors in comparison to the other methods.

compared to other methods. SITGAN yields lower performance than AD-DAE, with better performance than other baselines and the Naive baseline, reflecting a trend similar to the ADNI *Test Set* in Table 2. In contrast to the ADNI evaluation, BrLP performs better than DE-CVAE on all metrics in the OASIS setup, suggesting that BrLP’s latent diffusion-based formu-

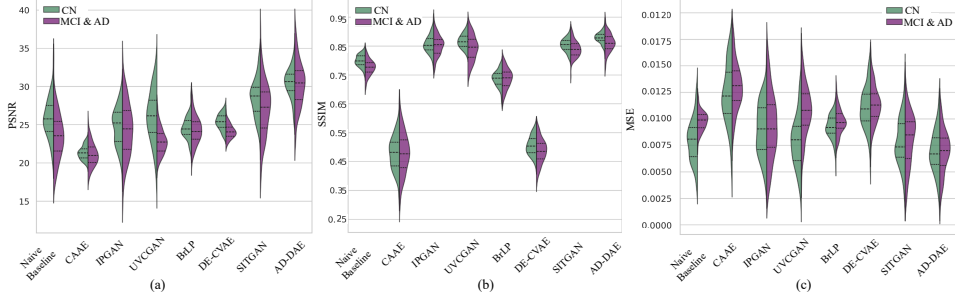


Figure 5: Left to right: Performance comparison of AD-DAE on *Cross-Data Setup* with baseline methods in terms of (a) PSNR, (b) SSIM, and (c) MSE. CN is shown in green and MCI & AD in violet, represented with their mean and first-quartile values. Across all metrics, AD-DAE demonstrates relatively better performance.

lation and explicit modeling of progression-related factors provide better generalization. For PSNR, both BrLP and DE-CVAE perform better than IPGAN and UVCGAN, whereas for MSE and SSIM, IPGAN and UVCGAN have better scores. This divergence can be attributed to the supervised nature of BrLP and DE-CVAE, which, during cross-dataset evaluation, exhibit greater deviations such as blurriness or alterations in subject-specific details. The performance of CAAE is relatively lower across all the scores. Overall, AD-DAE shows ***better generalization*** across different cognitive states and metrics.

5.4. Analysis of Volume Synthesis

To evaluate how well anatomical variations due to progression are captured, region-wise relative volumes between ground-truth and generated 3D images are compared, as described in Subsection 5.4.1. The qualitative analysis of these generated 3D volumes along the sagittal and coronal views is presented below in Subsection 5.4.2. Furthermore, deformations between the generated 3D images and the baseline are compared with ground truth using Jacobian analysis in Subsection 5.4.3. For the 2D models, estimated images (\hat{x}) are stacked, $\hat{X}_{:,:,d} = \hat{x}$ to generate the 3D images ($\hat{X} \in \mathbb{R}^{H \times W \times D}$, $d \in \{1, \dots, D\}$).

5.4.1. Region-wise Progression Analysis in 3D Volumes

The Table 3 reports region-based MAE between the relative volumetric changes of generated and ground-truth follow-up 3D volumes with respect to baseline, computed as $(V_{\hat{X}_f}^r - V_{X_b}^r)/(V_{X_b}^r)$ for generated follow-ups and

Table 3: Comparison of Mean Absolute Errors in Anatomical Regions Across Models Changing due to Progression. Region-wise mean errors are reported on *Test Set*. Statistical significance ($p < 0.01$) is indicated by asterisk (*).

Methods	MAE(↓)		
	Hippocampus	Amygdala	Lateral Ventricle
CAAE(Zhang et al., 2017)	0.4378 ± 0.1247	0.3625 ± 0.0837	0.6535 ± 0.6484
IPGAN(Xia et al., 2021)	0.3348 ± 0.0338	0.3283 ± 0.0260	0.5445 ± 0.5240
UVCGAN (Torbunov et al., 2023)	0.3288 ± 0.0307	0.2208 ± 0.0208	0.5453 ± 0.3540
BrLP(Puglisi et al., 2024)	0.1960 ± 0.0552	0.1731 ± 0.0529	0.3702 ± 0.1012
DE-CVAE(He et al., 2024)	0.1871 ± 0.0727	0.1183 ± 0.1117	0.1747 ± 0.1470
SITGAN(Wang et al., 2023)	0.1161 ± 0.0288	0.0211 ± 0.0201	0.1436 ± 0.1053
AD-DAE	$0.0282^* \pm 0.0281$	$0.0182^* \pm 0.0178$	$0.0405^* \pm 0.0391$

$(V_{X_f}^r - V_{X_b}^r)/(V_{X_b}^r)$ for ground truth, where r denotes the region of interest. AD-DAE achieves relatively lower MAE across all three regions, Hippocampus (0.0282), Amygdala (0.0182), and Lateral Ventricle (0.0405), with smaller standard deviations, indicating consistent modeling of progression-related volumetric changes. The errors are generally higher in the lateral ventricles than in the hippocampus and amygdala, reflecting the greater degree of ventricular change during progression. Among baselines, SITGAN exhibits lower errors, followed by DE-CVAE and BrLP. The higher errors in DE-CVAE relative to SITGAN stem from its supervised formulation, where progression is modeled without explicit control of anatomical change; as shown in Figure 3(g), DE-CVAE produces more ventricular enlargement than the ground truth. BrLP shows comparatively higher error, as although progression-related anatomical changes are captured in the latent space, translation to the image space does not faithfully reproduce precise image details. Overall, AD-DAE is able to better *capture* the *progression*-related changes at the *volumetric* level (3D), maintaining *inter-slice consistency*, although the generations of the model are at the slice level (2D).

To further validate whether anatomical changes are appropriately modeled, the normalized volumes of the hippocampus and lateral ventricles were plotted with age for MCI and AD categories using AD-DAE and the three better-performing baseline methods (SITGAN, DE-CVAE, BrLP). The normalized volumes for ground truth and generated follow-up, computed as $V_{X_f}^r/V_{X_b}^r$ and $V_{\hat{X}_f}^r/V_{\hat{X}_b}^r$ ($r \in$ Hippocampus, Lateral Ventricle), are presented in Figure 6. The quantitative findings from Table 3 align with these plots. Ground-truth normalized volumes are most closely followed by AD-DAE,

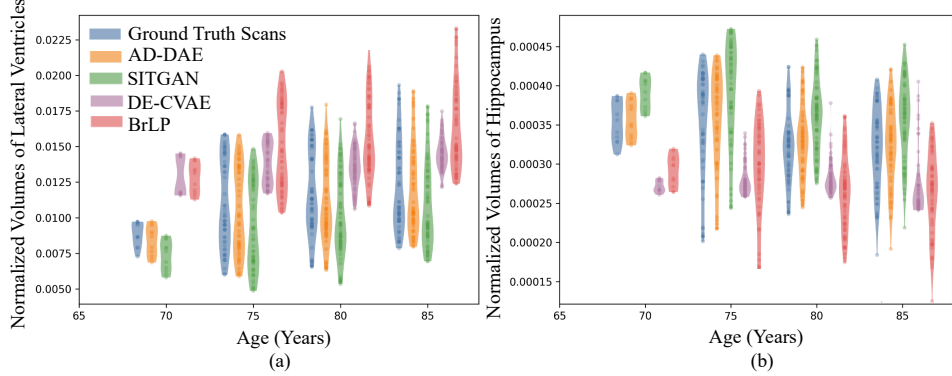


Figure 6: Left to right: Normalized volumes of (a) lateral ventricles and (b) hippocampus with age for generated volumes from AD-DAE, baseline methods, and ground truth, using subjects from MCI cognitive stage (*Test Set*). An overall increase in ventricular volume and a decrease in hippocampus volume are observed with age.

with SITGAN showing some deviations. Between DE-CVAE and BrLP, the former is closer to the ground truth in absolute values, whereas the latter is deviated the ground-truth error distribution. In the ventricles (Figure 6a), ground truth shows a clear increase with age, reflecting enlargement due to disease progression in MCI, a trend well followed by AD-DAE and broadly followed by other models. In the hippocampus (Figure 6b), ground truth shows an overall decrease with age, indicating atrophy, which is similarly reflected in the generated volumes. Overall, AD-DAE *closely follows* the ground-truth distribution of normalized volumes for both the *ventricular* and *hippocampus* regions.

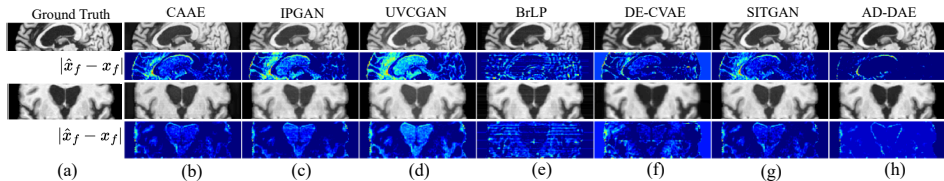


Figure 7: Left to right: (a) Ground truth images of sagittal and coronal view (b)–(h) Generated sagittal and coronal view from AD-DAE and baseline methods on the *Test Set* data. From top to bottom, the first and the third row represent images, while the second and the fourth highlight errors. AD-DAE shows relatively lower errors.

Table 4: Comparison of Jacobian of Ground Truth images ($J_{x_f \rightarrow x_b}$) with the predicted images ($J_{\hat{x}_f \rightarrow x_b}$) in terms of MAE. Region-wise mean Jacobian and errors are reported on *Test Set*.

Methods	Hippocampus		Amygdala		Lateral Ventricle	
	J_{Avg}	MAE	J_{Avg}	MAE	J_{Avg}	MAE
Ground Truth	0.9089	-	0.9642	-	1.2084	-
BrLP(Puglisi et al., 2024)	0.8778	0.0311	0.9048	0.0594	1.1125	0.0959
DE-CVAE(He et al., 2024)	0.9042	0.0047	0.9277	0.0365	1.1381	0.0703
SITGAN(Wang et al., 2023)	0.9058	0.0031	0.9637	0.0005	1.1327	0.0757
AD-DAE	0.9067	0.0022	0.9636	0.0006	1.1426	0.0658

5.4.2. Assessing Progression Across Views (Sagittal/ Coronal)

To assess the consistency of generation across other views, we present in Figure 7, (a) the ground truth and (b–h) the generated sagittal and coronal follow-up images along with residual errors, of a 77-year-old subject with MCI. The absolute error maps ($|\hat{x}_f - x_f|$) indicate that AD-DAE produces lower errors across both views, with errors generally higher in the sagittal plane compared to the coronal plane due to greater structural symmetry in coronal alignment. SITGAN exhibits higher errors than AD-DAE, particularly in the sagittal frontal lobe. For DE-CVAE and BrLP, errors are smaller in regions associated with progression-related changes but are higher in structures, such as sulcal folds. In the sagittal or coronal view, these models show better performance than other comparative models, as the 3D volumes are directly processed during modeling. The other comparative models (UVC-GAN, IPGAN, and CAAE) show errors in both progression-related and unrelated regions, with the frontal lobe being especially error-prone. Overall, from the view-wise error maps, it can be inferred that AD-DAE can **better reconstruct** the **other views** despite being modeled at the 2D slice level.

5.4.3. Are Anatomical Changes Captured in 3D Volumes?

In order to asses how well deformations are captured to transform base-line images (x_b) to follow-up images (\hat{x}_f), we compute the difference between the Jacobian determinant of generated volumes ($J_{\hat{X}_f \rightarrow X_b}$) and the ground truth ($J_{X_f \rightarrow X_b}$), as quantified in Table 4 in a region-wise manner. For each region, the average Jacobian determinant (J_{Avg} is average of voxels-wise values in $J_{\hat{X}_f \rightarrow X_b}$ or $J_{X_f \rightarrow X_b}$) is reported for ground truth and generated images, along with errors relative to ground truth. The hippocampus and amygdala exhibit $J_{Avg} < 1$, indicating atrophy, while the ventricular region shows $J_{Avg} > 1$, reflecting enlargement. All methods (BrLP, DE-CVAE,

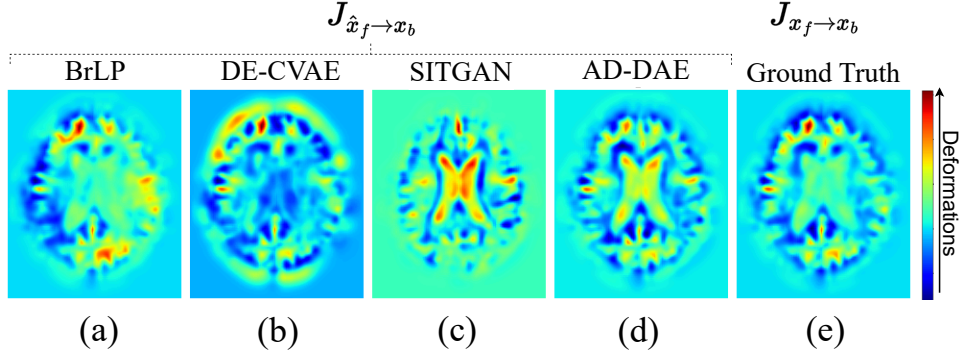


Figure 8: Left to right: Jacobian of (a)-(d) predicted follow-up images ($J_{\hat{x}_f \rightarrow x_b}$) and (e) ground truth follow-up image ($J_{x_f \rightarrow x_b}$) with the baseline image on the *Test Set* data.

SITGAN, AD-DAE) capture atrophy and enlargement patterns, with AD-DAE more accurately reflecting ground truth progression. Region-wise errors are highest for ventricles, followed by the hippocampus, then the amygdala, corresponding to the extent of change (ventricular enlargement exceeds hippocampal atrophy, which exceeds amygdala atrophy). AD-DAE achieves relatively lower errors and J_{Avg} closer to ground truth across all regions, followed by SITGAN, DE-CVAE, and BrLP. This highlights that the *non-linear deformations* in the image domain are well captured as *linear additive operation* within the *latent* representational *space* of AD-DAE.

These findings are supported by Figure 8, which visualizes Jacobian determinants for ground truth and each method. Higher values (enlargement) are depicted in reddish hues, and lower values (atrophy) in bluish hues. AD-DAE is able to model deformations in a relatively similar manner to the ground truth. AD-DAE and SITGAN show more precise deformation fields, while DE-CVAE and BrLP produce less localized, scattered deformations. Visual representations of *deformations* of AD-DAE are *closer* to the ground-truth deformations.

5.5. Downstream Analysis - Disease Classification

To evaluate the effectiveness of generated data (GD) relative to real data (RD), we trained an Alzheimer’s disease classifier with varying RD–GD ratios from the *Train Set* and tested it with RD from the *Test Set*. Figure 9 presents classification accuracy on *Test Set* when trained with varying RD-GD ratios. In the figure, the plots with dotted lines indicate accuracy when trained with generated data (GD) from AD-DAE and five comparison models, and the plot with a solid line indicates training with RD-only (0% GD).

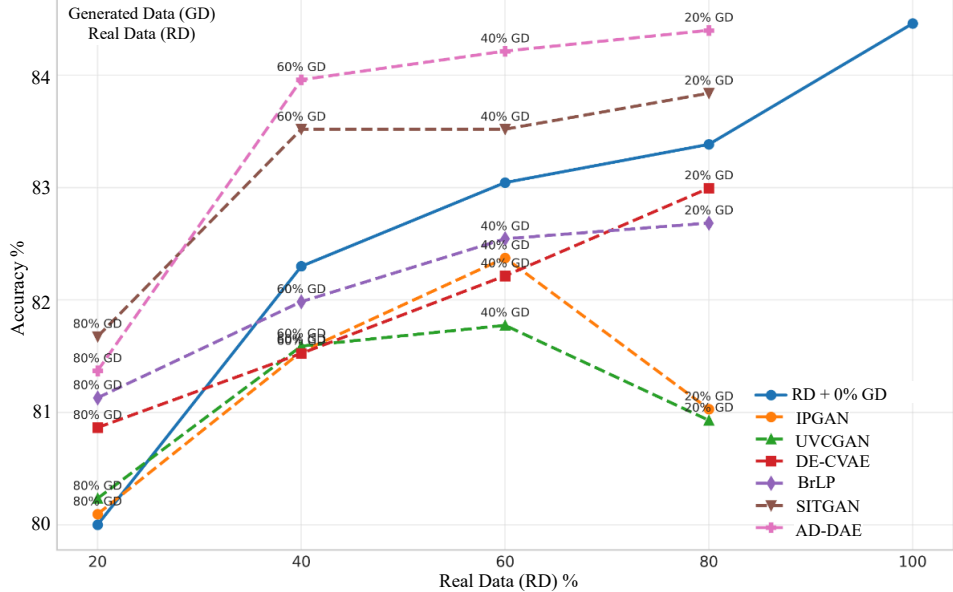


Figure 9: Plots comparing disease classification accuracy of AD-DAE and the baseline methods with variable ratios of Real Data (RD) and Generated Data (GD).

With RD-only (0% GD), accuracy increases monotonically with data size. At 20% RD + 80% GD, all models improve over the 20% RD baseline, though gains vary by method. At 40% RD + 60% GD, AD-DAE and SITGAN perform better than the RD-only (0% GD) baseline, while other models remain below. This trend is consistent at 60% RD + 40% GD, where AD-DAE maintains the higher accuracy compared to the other methods. With 80% RD + 20% GD, marginal improvements are observed, with AD-DAE, SITGAN, and BrLP sustaining accuracy above the RD-only setting.

Among the comparative models, SITGAN provides additional diversity to the training set but with comparatively lower performance. BrLP achieves stable progression modeling, though its latent diffusion design contributes less to image-level variability. DE-CVAE, despite showing better progression metrics than BrLP, exhibits limited improvement here due to fewer diverse samples generated by the VAE architectural formulation alone. The other GAN-based models have relatively lower performance. Overall, AD-DAE achieves relatively better performance across the RD-GD mixtures, indicating that *generated data effectively augments* the training distribution.

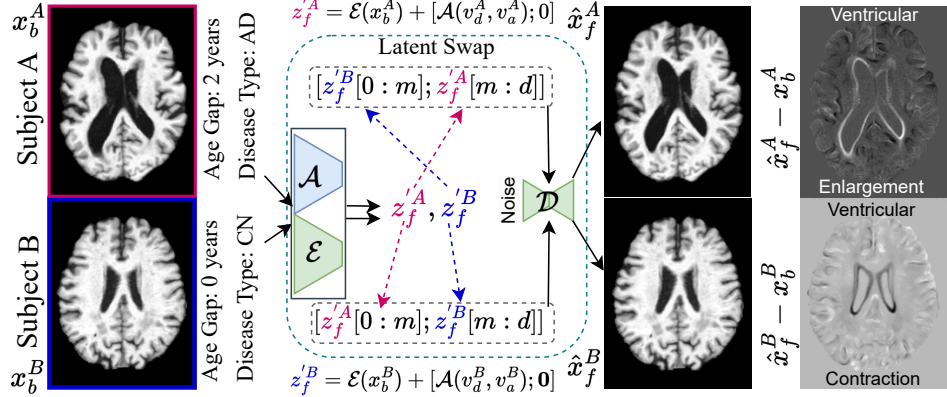


Figure 10: Architectural flow for generation of images by swapping the progression-related factors of the latent representation of two subjects to assess the disentanglement capability. Left to right: (i) Images from the two subjects, (ii) Latent generation with original cognitive status and age factors, (iii) Swapping of the 50 latent dimensions, and (iv) Generation with the swapped latents.

5.6. Latent Analysis

5.6.1. Are the factors of Progression Disentangled?

In order to evaluate how effectively AD-DAE disentangles progression-related factors from subject-specific identity, we performed a *latent swap* experiment in which the first m dimensions ($m = 50$) of the latent vectors were exchanged between two subjects prior to image generation. For experimentation, we have used the *Latent Swap Dataset*, consisting of paired CN and AD subjects. Specifically, the latent vector ($z_f^B = \mathcal{E}(x_b^B) + [\mathcal{A}(v_d^B, v_a^B); 0]$) of a CN subject (x_b^B) was swapped with the latent vector ($z_f^A = \mathcal{E}(x_b^A) + [\mathcal{A}(v_d^A, v_a^A); 0]$) of the paired AD subject (x_b^A). The resulting follow-up for x_b^A was generated from the modified latent $[z_f^B[0 : m]; z_f^A[m : d]]$, yielding \hat{x}_f^A . Similarly, $[z_f^A[0 : m]; z_f^B[m : d]]$ produced a new follow-up \hat{x}_f^B . This setup for one pair of subjects is illustrated in Figure 10.

Qualitative analysis from the Figure 10 shows that \hat{x}_f^A preserves the identity of x_b^A while exhibiting reverse progression effects, such as ventricular contraction in the residual image $\hat{x}_f^A - x_b^A$. This is consistent with the fact that the swapped progression attributes of x_b^B corresponded to CN with no age gap, in contrast to the original AD subtype and two-year gap of x_b^A . Similarly, \hat{x}_f^B incorporated the progression attributes of x_b^A and displayed ventricular enlargement indicative of AD progression.

For quantitative analysis, we have validated these observations across the

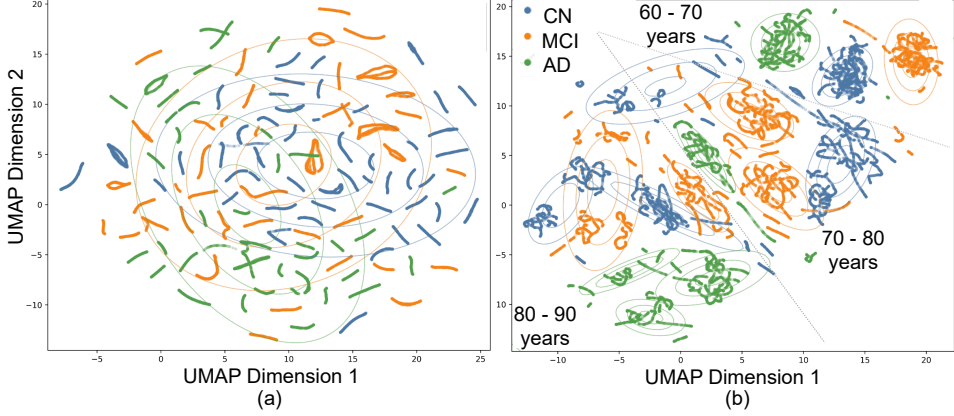


Figure 11: Left to right: Umap projections of (a) the entire latent representation ($z \in \mathbb{R}^d$) of images, and (b) the latent factors ($[z; 0], z \in \mathbb{R}^m$) having the age and cognitive status-related information.

full *Latent Swap Dataset* by measuring and comparing normalized ventricular volumes. For transformations from AD to CN with an age gap of two years or more at volume level, \hat{X}_f^A exhibited normalized volumes ($V_{\hat{X}_f^A}^r/V_{\hat{X}_f^A}$, $r \in$ Ventricular region) of 0.0105 compared to 0.0115 for X_b^A ($V_{X_b^A}^r/V_{X_b^A}$), indicating contraction. In contrast, for the transformation of CN to AD with an age gap of less than two, \hat{x}_f^B reached 0.0119 relative to 0.0105 in x_b^B , reflecting enlargement of ventricular structures. The computed PSNR values between \hat{x}_f^A and x_b^A is 26.01 dB and between \hat{x}_f^B and x_b^B is 25.86 dB, suggesting that subject identity is mostly preserved. These observations suggest that swapping the only progression-relevant factors of the latent **preserves subject identity** while **generating anatomical changes** related to the cognitive category and age progression, thereby achieving **disentanglement** in the latent space.

5.6.2. How Disentanglement affects Latent Space Organization?

To study the organization of the encoded latent representations (z) from AD-DAE and assess the role progression related factors, we projected these representations into a two-dimensional space using Umap (McInnes et al., 2018) as presented in Figure 11. The Umap projections of complete latent vectors ($z \in \mathbb{R}^d$) as shown in Figure 11 (a) highlight that the representations are not clearly separable, forming overlapping clusters. Gaussian Mixture

Model (GMM ⁶) based grouping by cognitive status produces broad ellipses with substantial overlap. In contrast, the projection of the first m dimensions ($[z; 0], z \in \mathcal{R}^m$) as in Figure 11 (b), reveals more distinct groupings. *Clusters align* primarily with *cognitive statuses*, with additional stratification by *age*. The GMM grouping in this space forms tight, well-separated clusters, with delineable ellipses particularly evident for subjects in the 60–70 year age range. At higher ages, clusters show increasing overlap, reflecting the compounding effects of normal aging in CN subjects and pathological progression in AD subjects. Overall, these results indicate that the first m dimensions of the latent representation embed cognitive status and age-related details, forming structures and organizing the latent space according to the embedded information.

5.7. Summary

Our image–diffusion–based modeling approach effectively *captures* the brain MRI distribution by encoding anatomical and progression-related information into a compact latent representational space and enabling *precise* control over image generation. This capability is reflected by the improvement in the image-level metrics and further supported by the consistency in volume-level progression generation. With volume-level analysis, we have shown that *non-linear* anatomical deformations between baseline and follow-up scans are closely approximated by simple *linear* additive transformations in the latent space of our model AD-DAE. Visual evaluations and latent swap experiments validate that disentangling identity- and progression-related factors in the latent space preserves subject-specific details.

Among the comparative modeling approaches, when progression-relevant factors are not explicitly disentangled, supervised methods generally perform better than unsupervised ones. Diffusion-based approaches better model the image distribution; however, for the latent diffusion-based models, generative fidelity is often constrained by the overall auto-encoding pipeline that controls image reconstruction quality. This highlights that *image diffusion* with *auto-encoding* formulation yields a semantically organized latent space, enabling unsupervised, progression-guided, and controlled image generation.

⁶<https://scikit-learn.org/stable/modules/generated/sklearn.mixture>

6. Conclusion

We have proposed a diffusion auto-encoder-based framework that models and generates the longitudinal progression of brain MRI images by encoding all relevant information into the latent representation space and enabling condition-controlled movements in this space, ensuring the disentanglement of progression and subject-identity related factors. The movements in the latent space are conditioned by the progression attributes and guided in an unsupervised manner, enforcing consistency between generated changes in the image space and the latent space. We have evaluated the performance of our model along with the comparative methods by comparing the closeness of progression generation with ground truth at the image and volumetric level across data sets (with 1016 subjects) and disease stages of Alzheimer's. We have further performed analysis in the latent space to validate how well our model disentangles progression and subject identity-related factors. *Limitations and Future Scope:* Our model currently integrates progression-awareness by conditioning with disease, age, and region-level information, which can be further extended to other clinical conditioning factors affecting Alzheimer's disease, like beta-amyloid ($A\beta$) accumulations, treatment-related, and textual report-based information associated with diseases. In summary, AD-DAE is shown to be effective in capturing the brain MRI distribution and enabling unsupervised, condition-controlled latent transitions to generate longitudinal progression images.

CRediT authorship contribution statement

Ayantika Das: Conceptualization, Data curation, Methodology, Software, Writing-original draft, Writing-review and editing. **Arunima Sarkar:** Methodology, Writing-review, and editing. **Keerthi Ram:** Conceptualization, Supervision, Writing-original draft. **Mohanasankar Sivaprakasam:** Funding acquisition, Project administration, Resources, Software, Supervision.

Funding

This work was supported by the Office of Principal Scientific Adviser, the Government of India, the Pratiksha Trust, and the Premji Invest.

Informed consent statement

There are no ethical implications regarding the public dataset.

Declaration of competing interest

The authors declare that they have no Conflict of interest.

Acknowledgments

The authors would like to thank the entire team at Sudha Gopalakrishnan Brain Centre, IITM, for their consistent support. Data collection and sharing for this project was funded by the Alzheimer's Disease Neuroimaging Initiative (ADNI) (National Institutes of Health Grant U01 AG024904) and DOD ADNI (Department of Defense award number W81XWH-12-2-0012).

References

G. M. McKhann, D. S. Knopman, H. Chertkow, B. T. Hyman, C. R. Jack Jr, C. H. Kawas, W. E. Klunk, W. J. Koroshetz, J. J. Manly, R. Mayeux, et al., The diagnosis of dementia due to alzheimer's disease: recommendations from the national institute on aging-alzheimer's association workgroups on diagnostic guidelines for alzheimer's disease, *Alzheimer's & dementia* 7 (2011) 263–269.

C. R. Jack Jr, J. S. Andrews, T. G. Beach, T. Burachio, B. Dunn, A. Graf, O. Hansson, C. Ho, W. Jagust, E. McDade, et al., Revised criteria for diagnosis and staging of alzheimer's disease: Alzheimer's association workgroup, *Alzheimer's & Dementia* 20 (2024) 5143–5169.

J. Barnes, J. W. Bartlett, L. A. van de Pol, C. T. Loy, R. I. Scahill, C. Frost, P. Thompson, N. C. Fox, A meta-analysis of hippocampal atrophy rates in alzheimer's disease, *Neurobiology of aging* 30 (2009) 1711–1723.

J. Ashburner, K. J. Friston, Voxel-based morphometry—the methods, *Neuroimage* 11 (2000) 805–821.

B. Sauty, S. Durrleman, Progression models for imaging data with longitudinal variational auto encoders, in: International conference on medical image computing and computer-assisted intervention, Springer, 2022, pp. 3–13.

G. Marti-Juan, M. Lorenzi, G. Piella, A. D. N. Initiative, et al., Mc-rvae: multi-channel recurrent variational autoencoder for multimodal alzheimer's disease progression modelling, *NeuroImage* 268 (2023) 119892.

T. Xia, A. Chartsias, C. Wang, S. A. Tsafaris, A. D. N. Initiative, et al., Learning to synthesise the ageing brain without longitudinal data, *Medical Image Analysis* 73 (2021) 102169.

C. J. Wang, N. S. Rost, P. Golland, Spatial-intensity transforms for medical image-to-image translation, *IEEE transactions on medical imaging* 42 (2023) 3362–3373.

G. Pombo, R. Gray, M. J. Cardoso, S. Ourselin, G. Rees, J. Ashburner, P. Nachev, Equitable modelling of brain imaging by counterfactual augmentation with morphologically constrained 3d deep generative models, *Medical Image Analysis* 84 (2023) 102723.

L. Puglisi, D. C. Alexander, D. Ravì, Enhancing spatiotemporal disease progression models via latent diffusion and prior knowledge, in: *International Conference on Medical Image Computing and Computer-Assisted Intervention*, Springer, 2024, pp. 173–183.

K. Preechakul, N. Chatthee, S. Wizadwongsa, S. Suwajanakorn, Diffusion autoencoders: Toward a meaningful and decodable representation, in: *Proceedings of the IEEE/CVF conference on computer vision and pattern recognition*, 2022, pp. 10619–10629.

D. A. Hudson, D. Zoran, M. Malinowski, A. K. Lampinen, A. Jaegle, J. L. McClelland, L. Matthey, F. Hill, A. Lerchner, Soda: Bottleneck diffusion models for representation learning, in: *Proceedings of the IEEE/CVF Conference on Computer Vision and Pattern Recognition*, 2024, pp. 23115–23127.

Y. Zhao, B. Ma, P. Jiang, D. Zeng, X. Wang, S. Li, Prediction of alzheimer's disease progression with multi-information generative adversarial network, *IEEE Journal of Biomedical and Health Informatics* 25 (2020) 711–719.

D. Ravi, S. B. Blumberg, S. Ingala, F. Barkhof, D. C. Alexander, N. P. Oxtoby, A. D. N. Initiative, et al., Degenerative adversarial neuroimage nets for brain scan simulations: Application in ageing and dementia, *Medical Image Analysis* 75 (2022) 102257.

E. Jung, M. Luna, S. H. Park, Conditional gan with an attention-based generator and a 3d discriminator for 3d medical image generation, in: *International Conference on Medical Image Computing and Computer-Assisted Intervention*, Springer, 2021, pp. 318–328.

R. He, G. Ang, D. Tward, A. D. N. Initiative, Individualized multi-horizon mri trajectory prediction for alzheimer's disease, in: *International Conference on Medical Image Computing and Computer-Assisted Intervention*, Springer, 2024, pp. 26–37.

Z. Zhang, Y. Song, H. Qi, Age progression/regression by conditional adversarial autoencoder, in: *Proceedings of the IEEE conference on computer vision and pattern recognition*, 2017, pp. 5810–5818.

E. Jung, M. Luna, S. H. Park, Conditional gan with 3d discriminator for mri generation of alzheimer's disease progression, *Pattern Recognition* 133 (2023) 109061.

J. Kapoor, J. H. Macke, C. F. Baumgartner, Mrextrap: Linear prediction of brain aging in autoencoder latent space of mri scans, in: *Medical Imaging with Deep Learning*, 2024.

K. Zhang, G. Chen, S. Huang, F. Zhu, Z. Ding, D. Shen, Development-driven diffusion model for longitudinal prediction of fetal brain mri with unpaired data, *IEEE Transactions on Medical Imaging* (2024).

J. S. Yoon, C. Zhang, H.-I. Suk, J. Guo, X. Li, Sadm: Sequence-aware diffusion model for longitudinal medical image generation, in: *International Conference on Information Processing in Medical Imaging*, Springer, 2023, pp. 388–400.

M. Litrico, F. Guarnera, M. V. Giuffrida, D. Ravì, S. Battiato, Tadm: Temporally-aware diffusion model for neurodegenerative progression on brain mri, in: International Conference on Medical Image Computing and Computer-Assisted Intervention, Springer, 2024, pp. 444–453.

B. Kim, J. C. Ye, Diffusion deformable model for 4d temporal medical image generation, in: International Conference on Medical Image Computing and Computer-Assisted Intervention, Springer, 2022, pp. 539–548.

B. Kim, I. Han, J. C. Ye, Diffusemorph: Unsupervised deformable image registration using diffusion model, in: European conference on computer vision, Springer, 2022, pp. 347–364.

Y. Dalva, P. Yanardag, Noiseclr: A contrastive learning approach for unsupervised discovery of interpretable directions in diffusion models, in: Proceedings of the IEEE/CVF conference on computer vision and pattern recognition, 2024, pp. 24209–24218.

P. Dhariwal, A. Nichol, Diffusion models beat gans on image synthesis, *Advances in neural information processing systems* 34 (2021) 8780–8794.

Z. Zhang, Z. Zhao, Z. Lin, Unsupervised representation learning from pre-trained diffusion probabilistic models, *Advances in neural information processing systems* 35 (2022) 22117–22130.

A. Das, M. Chaudhuri, K. Bhat, K. Ram, M. Bota, M. Sivaprakasam, Posdiffae: Position-aware diffusion auto-encoder for high-resolution brain tissue classification incorporating artifact restoration, *IEEE Journal of Biomedical and Health Informatics* (2025).

J. Ho, A. Jain, P. Abbeel, Denoising diffusion probabilistic models, *Advances in neural information processing systems* 33 (2020) 6840–6851.

A. Q. Nichol, P. Dhariwal, Improved denoising diffusion probabilistic models, in: International conference on machine learning, PMLR, 2021, pp. 8162–8171.

Y. Huang, J. Huang, Y. Liu, M. Yan, J. Lv, J. Liu, W. Xiong, H. Zhang, L. Cao, S. Chen, Diffusion model-based image editing: A survey, *IEEE Transactions on Pattern Analysis and Machine Intelligence* (2025).

Y. Zhang, Y. Song, J. Liu, R. Wang, J. Yu, H. Tang, H. Li, X. Tang, Y. Hu, H. Pan, et al., Ssr-encoder: Encoding selective subject representation for subject-driven generation, in: Proceedings of the IEEE/CVF Conference on Computer Vision and Pattern Recognition, 2024, pp. 8069–8078.

P. Li, R. Wang, H. Huang, R. He, Z. He, Pluralistic aging diffusion autoencoder, in: Proceedings of the IEEE/CVF international conference on computer vision, 2023, pp. 22613–22623.

Z. Lu, C. Wu, X. Chen, Y. Wang, L. Bai, Y. Qiao, X. Liu, Hierarchical diffusion autoencoders and disentangled image manipulation, in: Proceedings of the IEEE/CVF Winter Conference on Applications of Computer Vision, 2024, pp. 5374–5383.

Z. Yue, J. Wang, Q. Sun, L. Ji, E. I.-C. Chang, H. Zhang, Exploring diffusion time-steps for unsupervised representation learning, in: The Twelfth International Conference on Learning Representations, 2024.

J. Song, C. Meng, S. Ermon, Denoising diffusion implicit models, arXiv preprint arXiv:2010.02502 (2020).

B. Billot, D. N. Greve, O. Puonti, A. Thielscher, K. Van Leemput, B. Fischl, A. V. Dalca, J. E. Iglesias, et al., Synthseg: Segmentation of brain mri scans of any contrast and resolution without retraining, Medical image analysis 86 (2023) 102789.

S. Xie, R. Girshick, P. Dollár, Z. Tu, K. He, Aggregated residual transformations for deep neural networks, in: Proceedings of the IEEE conference on computer vision and pattern recognition, 2017, pp. 1492–1500.

C. R. Jack Jr, M. A. Bernstein, N. C. Fox, P. Thompson, G. Alexander, D. Harvey, B. Borowski, P. J. Britson, J. L. Whitwell, C. Ward, et al., The alzheimer's disease neuroimaging initiative (adni): Mri methods, Journal of Magnetic Resonance Imaging: An Official Journal of the International Society for Magnetic Resonance in Medicine 27 (2008) 685–691.

P. J. LaMontagne, T. L. Benzinger, J. C. Morris, S. Keefe, R. Hornbeck, C. Xiong, E. Grant, J. Hassenstab, K. Moulder, A. G. Vlassenko, et al., Oasis-3: longitudinal neuroimaging, clinical, and cognitive dataset for normal aging and alzheimer disease, medrxiv (2019) 2019–12.

F. Isensee, M. Schell, I. Pflueger, G. Brugnara, D. Bonekamp, U. Neuberger, A. Wick, H.-P. Schlemmer, S. Heiland, W. Wick, et al., Automated brain extraction of multisequence mri using artificial neural networks, Human brain mapping 40 (2019) 4952–4964.

R. T. Shinohara, E. M. Sweeney, J. Goldsmith, N. Shiee, F. J. Mateen, P. A. Calabresi, S. Jarso, D. L. Pham, D. S. Reich, C. M. Crainiceanu, et al., Statistical normalization techniques for magnetic resonance imaging, NeuroImage: Clinical 6 (2014) 9–19.

D. Torbunov, Y. Huang, H. Yu, J. Huang, S. Yoo, M. Lin, B. Viren, Y. Ren, Uvcgan: Unet vision transformer cycle-consistent gan for unpaired image-to-image translation, in: Proceedings of the IEEE/CVF winter conference on applications of computer vision, 2023, pp. 702–712.

L. McInnes, J. Healy, N. Saul, L. Großberger, Umap: Uniform manifold approximation and projection, J. Open Source Softw. 3 (2018) 861.